DTU Library

A computational efficient algorithm for the aerodynamic response of non-straight blades

Gaunaa, Mac; Réthoré, Pierre-Elouan Mikael; Sørensen, Niels N.; Døssing, Mads

Link back to DTU Orbit

A computationally efficient algorithm for the aerodynamic response of non-straight blades

Mac Gaunaa, Pierre-Elouan Réthoré, Niels N. Sørensen and Mads Døssing
Wind Energy Department, Risø National Laboratory, DTU, DK-4000 Roskilde, Denmark
macg@risoe.dtu.dk

1   Introduction

The work presented in this work highlight the performance of different computational models, which are all able to take into account the main effects of using non-straight blades and blades being non-orthogonal to the axis of rotation (coned rotors) on horizontal axis wind turbines. Specifically emphasis is on the performance of the computationally lighter models, which are both based on the lifting line theory. These two methods are the free wake model and the compytationally relatively light prescribed wake model.

For the application on horizontal axis wind turbines, non straight blades (or coned rotors) can be applied for several reasons. Winglets, for instance, can be applied to increase the power production without increasing the swept area. Swept blades can be beneficial for passive load reduction on the rotors. Since the winglet case cannot be predicted even close to physically correct using the preferred method for load calculations (and most design calculations) used in industry, the BEM based codes, this case will be investigated in the present work.

For the application of winglets on horizontal-axis wind turbines, previous works has been done by Van Bussel [2], Imamura et al. [10], Johansen et.al. [13, 14], Gaunaa and Johansen [5–7] and Chattot [3]. Van Bussel [2] developed a momentum theory for winglets on horizontal-axis wind turbines, explaining the positive effect of a winglet on a rotor by the downwind shift of the wake vorticity. This result was, later shown to be incorrect by Gaunaa and Johansen [5]. The works by Imamura et al. [10] and Johansen et.al. [13, 14] are numerical in nature, as the former work is based on a free-wake vortex-lattice method. The work of Johansen et.al. is based on Navier-Stokes simulations with the CFD code EllipSys3D, and predicts an increase in CP of 1.74% on a modern MW sized turbine. Gaunaa and Johansen's

work [5–7] included their explanation of the main principle for power augmentation by the use of winglets: a reduction of tip effects. That work further employed a free wake method to optimize power production for rotors with winglets of different sizes. Using this approach the power production on a rotor with winglets of length $\Delta l/R = 0.02$ was increased 2.2%[1] compared to a non-wingletted rotor designed for maximum power output [11]. The simulations further showed that downwind winglets performed better than their upwind counterparts. Johansen et.al. [12] further investigated off-design performance of rotors with winglets. The work of Chattot [3] is based on the Goldstein approach, where each blade is treated as a lifting line generating a helicoidal vortex sheet, along prescribed helices whose pitch is determined to satisfy the wake equilibrium condition. This work included also the effect of sweep and dihedral of the winglet, and used the NREL blade as the point of reference. It was found that the backward swept winglets performed better than the forward swept ones. Along the same lines as for the non-rotating case, the main purpose of adding a winglet to a wind turbine rotor is to reduce tip-losses more than the increase in viscous surface drag corresponding to the increased surface area and thereby increase the aerodynamic efficiency of the turbine. The use of winglets on rotors other than wind energy applications was performed by Müller & Staufenbiel [21] and Müller [22], and deals with using winglets on helicopters.

The design codes and load computation codes used in the wind turbine industry are for the vast majority based on Blade Element Momentum (BEM) theory, which can not take the effects of nonplanar rotors into account due to the assumption of annularly independent streamtubes. One method that can take all these effects into account is for instance

---

[1] The power production was evaluated using the CFD code EllipSys3D using the rotor geometry obtained from the free wake code results.

Navier-Stokes CFD methods [13, 14]. The drawback with this type of method lie in it's computational cost, which limits this methods' use in the design process. Another method which can include correctly the effect a winglet has on the aerodynamic response of the rotor is free wake vortex based methods. These methods are, however, also too computationally costly for use in for instance fatigue load calculations. Additionally, the free wake methods are generally numerically relatively unstable by nature, which usually require a great deal of attention from the user. One viable type of methods that could provide the desired combination of accuracy, numerical stability and computational speed could be the prescribed wake models. However, the wake shape depends on tip speed ratio, bound circulation as well as the geometry of the rotor (winglet length/direction). This was investigated in by Gaunaa et.al. [8]. In this work it was shown that the performance of the prescribed wake model can be very close to that of the the free wake model if the model is not used too far from where it was tuned to imitate the behavior of the free wake model.

Previous work with lifting line methods by the present authors have all used the basic formulation, where the bound circulation is prescribed, and the local blade loading is found from the relative velocities. In the current work, this framework is extended such that the value of the bound circulation is determined by coupling 2D airfoil lift coefficients, induced velocities and knowledge about the orientation of the airfoil sections relative to the rotor. This way we have a lifting line based tool (either based on the free wake or the prescribed wake engine) which can determine the loading on rotors of any shape including non-planar configurations. Validation of this model against the results from Johansen & Sørensen [15], where the effect of adding up- and downwind winglets to an existing design of a modern rotor is assessed, will be given.

With a lifting line method, which can handle arbitrary rotor geometries, the solution for a given bound circulation is essentially the induced velocities, from which the loadings may be determined subsequently. An interesting possibility is then that a 3D layout of a rotor, which may then be non-planar, can be determined based on this information, because the airfoil sections should just be scaled and positioned such that their angles of at-

tack is as specified by the user, and that their chordlength is such that the corresponding loading corresponds to the given bound circulation and relative flow velocity. During the present project, a tool which determines the 3D rotor surface based on the free wake lifting line results has been developed. The performance of rotors with and without winglets designed using this method will be analyzed with the 3D CFD code EllipSys3D [19, 20, 26] to investigate how well this design method works.

Following this introduction, the basic methods used in the work are presented, after which several key results mentioned above, obtained with the models are shown. The last section contains the main conclusions of this work as well as suggestions for further work.

2 Computational models

2.1 Lifting line free wake model

2.1.1 Baseline version: prescribed bound circulation

In the Free-Wake Lifting Line method used in the present work, the wings are represented by concentrated line vortices, from which shed vorticity emanates into the wake. The method does not take into consideration the actual local geometry of the wing cross-section (airfoil shape), but models only the effect of the circulations that the airfoils generate. The inviscid lift forces from the fluid on the wings are evaluated from the Kutta-Joukowski Theorem, $\vec{L} = \rho \vec{V}_{rel} \times \vec{\Gamma}$, using the relative velocity of the flow with respect to the wings, including also the contributions from the free wakes of the wings. Since viscous effects are not naturally a part of a lifting line algorithm, they are taken into account separately. The local drag forces act in the direction of the relative flow direction, and the magnitudes are obtained from the lift forces using 2D lift-to-drag ratios of the airfoil sections. An algorithm for evaluating the induced forces from the velocities that the nonplanar bound vorticity induces on itself is included in the model. In order to avoid the lifting line singularity on itself, this extra induced velocity is computed using a vortex-lattice type grid. The self-induced velocities are obtained using an iterative scheme using a weighted difference between 3D and 2D self-induced velocities. From the converged self-induced velocity, the induced forces are computed using the

lifting line. The self-induced forces in the case of winglets straight up- or down-wind produces negligible changes in power production. A non-negligible effect on power production from this term is only seen in cases where the winglets have sweep, i.e. where the winglets are tilted forward or backward. Since the winglets considered in the present work have no sweep, the self-induced effect will not be discussed further. In order to determine the shape of the free wake, a steady-state free wake method was adopted. Due to the inherent unstable nature of free wake methods for wind turbine applications, some care must be taken to obtain converging solutions. Since the freestream velocity is constant, and the turbine is assumed not to be operating in yawed conditions, only the vortices from one wing need be updated; the other ones are obtained from symmetry conditions. In order to ensure adequate resolution of the wake, the position of the wake is determined in specific planes parallel to the rotor plane, with narrow spacing near the rotor plane and increased spacing further down the wake (ΔZ=0.003R at the rotor disc and ΔZ=0.009R at Z=3R using 450 cross-sections). In the first part of the wake (up to 3R), the wake is updated freely, and the wake velocities are evaluated at the intersection between the linear vortex elements. In the second part of the wake, the vortex strings keep constant radial distance to the rotational axis, and the azimuthal positions are obtained from extrapolation of the values at the end of the free wake zone. The last zone is a semi-infinite vortex tube to model the effect of the far wake. The positions of the free wake are updated for one cross-section at the time, and the differences in radial and azimuthal positions are convected to all downstream coordinates of the wake after updating all positions at that specific axial position. In order to avoid stability problems with the free wake method, the cross-sections are not updated in the typically parabolic marching fashion, but according to a scheme that ensures that the update cross-section position varies as much as possible in space while still covering all cross-sections in the free wake domain during a single global iteration. This scheme is an adoption of the integer sequence A049773 in the on-line encyclopedia of integer sequences [32]. Furthermore, relaxation is employed to facilitate a more stable numerical behavior. The relaxation coefficient used for the present computations was set to 0.6. The wake vorticity

is modeled by rectilinear vortices with a viscous Rankine vortex core: 0.01R at rotor disc going toward 0.05R exponentially with a half-distance of 2R. The results shown in this work were all obtained with the bound vorticity along the main wings discretized in 40 elements, with finer resolution towards root and tip where gradients are steeper. The winglet part of the wings was discretized using an additional 10 elements. Investigations of the discretization have shown that the present setup produces results that change only marginally by further increasing resolution. The integral forces and dimensionless numbers are obtained from integration of the total distributed forces.

A validation of the main part of the code in a non-winglet setting is found in Johansen [11], where comparison of a priori results obtained with the current code and an actuator disc code were made with results from the full 3D CFD code EllipSys3D [19, 20, 26] on an aerodynamically optimal rotor. The agreement between CFD and free wake method results was excellent. please refer to [11] for the details. For a comparison of the results from the free wake method with EllipSys3D for rotors including winglets also very good agreement was observed. Please refer to [6] for the details on the comparison between CFD and the free wake results in the wingletted case.

2.1.2 Prediction tool using geometry and 2D airfoil coefficients

As a part of the present project, a prediction tool based on the basic free wake lifting line code has been implemented, in which the bound circulation corresponding to the rotor geometry and 2D airfoil coefficients is determined iteratively based on the relative velocity obtained from the free wake code. The rotor geometry is defined using the spanwise direction, chordlength (defined in the direction perpendicular to the spanwise direction) and orientation of the chordwise direction in space. The coupling is determined by equating the lift per spanwise length from the definition

$$l = \frac{1}{2}\rho V_{rel,norm}^2 c C_l(\alpha_{rel,norm}) \qquad (1)$$

with the lifting part from the Joukowski equation

$$l = |\bar{l}| = |\rho \bar{V}_{rel} \times \bar{\Gamma}_B| = \rho V_{rel,norm} \Gamma_B \quad (2)$$

Note that, in accordance with what is found from panel solution of a wing with no spanwise

variations in load, we have to use only the component of the relative velocity perpendicular to the spanwise direction,

$$V_{rel,norm} = |\bar{V}_{rel,norm}| = |\bar{V}_{rel} - \bar{V}_{rel} \cdot \bar{e}_{span}|, \tag{3}$$

as well as the 2D angle of attack defined as the angle from the chord-direction[2], $\bar{e}_{chord}$, to the relative velocity vector projected onto the plane perpendicular to the spanwise direction, $\bar{V}_{rel,norm}$.

$$\alpha_{rel,norm} = \arctan \frac{\overbrace{(\bar{e}_{chord} \times \bar{e}_{span})}^{\bar{e}_{normal}} \cdot \bar{V}_{rel}}{\bar{e}_{chord} \cdot \bar{V}_{rel}} \tag{4}$$

The result from this is that the bound circulation can be determined from Equation (5) below

$$\Gamma_B = \frac{1}{2} V_{rel,norm} c C_l(\alpha_{rel,norm}) \tag{5}$$

With this determination of the bound circulation, it is possible to determine the aerodynamic loading on any planar or non-planar rotor based on the geometric layout, operating parameters and 2D airfoil coefficients. Since the equations from which the bound circulation is updated remain the same, the coupling algorithm can be used equally well in the prescribed wake case too.

2.2 Lifting line prescribed wake model

2.2.1 Baseline version: prescribed bound circulation

The baseline version of the prescribed wake model developed in this project is described in detail in Gaunaa et.al. [8] along with a simpler prescribed wake model. Since the results obtained with the slightly more advanced model was superior to those of the simpler model, only the model that obtained the best results will be shown here.

The prescription function and method in the prescribed wake model is based on a number of baseline results from the steady free wake code, which have earlier given results in very good agreement with CFD results for both standard rotor cases [11] and rotors with winglets [5–7]. The free wake code was used

to simulate a number of rotor geometries with different bound circulations/loadings, and from these results to formulate and subsequently test, the bounds of application of the prescribed wake model. The integral results from these baseline free wake solutions are shown in [8].

The prescribed wake model reflects key features found in the free wake solutions: wake expansion, the outermost vortex filaments being convected faster than the inner ones, modeling tangential induction, varying axial transport velocity through the wake. In order to keep the model in as simple a form possible, the model still only uses the integral quantity C_T and winglet size and orientation in the formulation. The model for the main part of the wake basically consist of two parts: the first one expressing the radial expansion of the wake, and the second part expresses the pitch angle of the trailed vortex filaments throughout the wake. The first part of the model is given by Equations (6) to (9)

$$f_1(C_T) = 1.0 - 0.715^{-20.5\,C_T + 25.9} \tag{6}$$

$$f_2(\Delta Z) = 1.073(1.0 - \exp(-0.91\Delta Z))^{0.88} \tag{7}$$

$$(r_i/R)_{FW}(C_T) = f_1\sqrt{0.5(1/\sqrt{(1-C_T)}+1)} \tag{8}$$

$$(r_i/R)(\Delta Z, C_T) = ((r_i/R)_{FW} - (r_i/R)_{Rotor})f_2 + (r_i/R)_{Rotor} \tag{9}$$

The function f_1 expresses the deviation of the free wake far field radial expansion from what would be expected from 1D momentum theory, given the thrust coefficient. The other function, f_2, expresses the radial expansion as a function of downstream distance, and is fitted the results from the free wake results.

The other part of the model, which deal with the pitch angle of the trailed vortex filaments throughout the wake, is easiest described by treating the axial transport velocity and the tangential induction separately, and then combining the the two to finally get the pitch angle of the vortex filaments. The axial transport velocity correspond to the radial expansion in Equation (9), and can be expressed as in Equations (10) to (13), in terms of an local axial induction factor defined as commonly done in 1D momentum and BEM theory: $V_{ax} = V_\infty(1 - a_{loc})$

$$\tilde{a}(C_T) = 0.5 - 0.5\sqrt{1-C_T} \tag{10}$$

$$a_{basis}(C_T, \Delta Z) = 1$$
$$-\tilde{a}(1/(f_2(f_1\sqrt{(1/\sqrt{1-C_T}+1)/2}-1)+1))^2$$
$$(11)$$

Further, in order to take into account the faster convection of the tip vortices, all vortices trailed from positions outside of $r/R = 0.9$ have a reduced induction factor: the axial induction factor for these vortices are reduced to a value lower than the "basis" value all along the filaments. So for the "inner" vortex filaments the local axial induction is given by

$$a_{loc,inner}(C_T, \Delta Z) = a_{basis}(C_T, \Delta Z) \quad (12)$$

Correspondingly the "outer" vortex filaments the local axial induction is given by

$$a_{loc,outer}(C_T, \Delta Z) = K_B(l_{wl})a_{basis}(C_T, \Delta Z)$$
$$(13)$$

As indicated, the value of the constant K_B depends only on the winglet length, and has been tuned to match the power production for the 'high' loaded case for $\lambda = 8$. The values corresponding to the different winglet lengths are given in Table 1. In fact, the vortices trailed closest to the innermost portion of the blade are also convected faster downstream, corresponding to what happens in the tip section. This is, however, not included in the present model, because it was found that the influence from including this effect in the model has a negligible effect on both the power production and the loads.

The tangential induction is modeled using the result from vortex tube modeling (see the works by Øye and co-workers in [17, 31]), where it can be shown that the tangential induction in the wake has the magnitude corresponding exactly to the influence of a root vortex having the same strength as the bound vortex strength from all wings at the same position on the wings from where the vorticity filament was trailed. Combining this result with the expressions for the axial convection velocity above, we get for the derivative of the azimuth coordinate of the wake filaments with respect to downwind coordinate

$$\frac{d\Theta}{dz}(C_T, \Delta Z, \lambda, N_B, \Gamma_{B,i}) =$$
$$-(\frac{\lambda}{R} + \frac{N_B\Gamma_{B,i}}{2\pi V_\infty(r_i/R)^2})/(1-a_{loc}) \quad (14)$$

Note, that the coordinate system in which the wake positions are described follows the rotor.

Therefore, the first term in Equation (14) correspond to the relative tangential velocity due to the rotation of the rotor, while the second term correspond to the actual induced tangential velocity in the wake as seen from a "ground based" observer.

Once the radial expansion and trailed vortex filament pitch angles are determined from Equations (9) and (14), the wake vortex system can be constructed, and the induced velocities, etc. can be determined from them.

2.2.2 Prediction tool using geometry and 2D airfoil coefficients

Since the method for finding the bound circulation that corresponds to a given rotor layout, 2D aerodynamic coefficients and operation parameters are identical to one described in the free wake code section with the prescribed wake method put in stead of the free wake method, the coupling method is identical. Please refer to section 2.1.2 for the details.

Note also that when the prescribed wake method is implemented in a tool where the geometry of the rotor is given, the determination of a wake corresponding to the loading situation (thrust coefficient) will require iteration, since the bound circulation, and from these the thrust coefficient, will depend on the induced velocities, which in turn depend on the thrust coefficient.

2.3 Single point aerodynamic rotor design using lifting line methods

It is fairly straightforward to generate the "aerodynamic" 3D surface corresponding to a solution resulting from either the free wake code or the prescribed wake code for a given prescribed bound circulation. After choosing the airfoils to be put on the rotor, the design angles of attack, α_{design}, are chosen (based on 2D airfoil performance). From this the design lift coefficient is found from 2D airfoil polars $C_{l,design} = C_{l,2D}(\alpha_{design})$. From the lifting line solution, the velocities relative to the rotor blades are known. Based on this information, it is now possible to determine $V_{rel,norm}$ from Equation (3), and from this to determine the chordlenght from Equation (5) as

$$c = \frac{2\Gamma_B}{V_{rel,norm}C_{l,design}} \quad (15)$$

Table 1: Values for K_B as function of nondimensional winglet length l_{wl}/R.

l_{wl}/R	-0.10	-0.08	-0.06	-0.04	-0.02	0.00	0.02	0.04	0.06	0.08	0.10
K_B	0.419	0.426	0.441	0.458	0.478	0.511	0.469	0.450	0.438	0.435	0.423

Furthermore, the orientation of the chordlength in space can be determined from Equation (4), remembering that the "chordwise direction", $\bar{e}_{chord}$, is in the plane perpendicular to the spanwise direction.

Even though from a lifting line viewpoint the circular root section has no function, most wind turbine manufacturers would probably argue that there is use for a root section to connect the aerodynamic effective part of the rotor to transfer the driving torque to the rest of the wind turbine. Therefore, an algorithm morphing the aerodynamically active part of the rotor nicely into a circular crosssection at the blade root was developed. The result of adding this is shown in Figure (1).
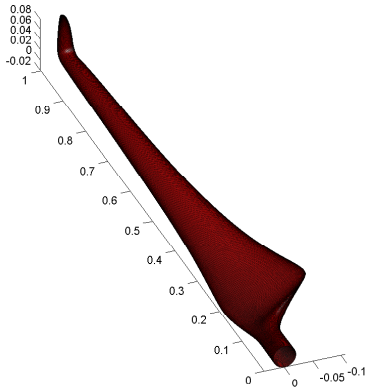

Figure 1: *Example of total 3D blade surface following from the high loading case with a tip speed ratio of 8 and a downwind winglet length of 8% of the radius.*

2.4 Computational Fluid Dynamics: EllipSys3D

2.4.1 Method

The in-house flow solver EllipSys3D [19, 20, 26, 27] is used in all CFD computations presented in the following. The EllipSys3D code is a multiblock finite volume discretization of the incompressible Reynolds-averaged Navier-Stokes (RANS) equations in general curvilin-ear co-ordinates. The code uses a collocated variable arrangement, and Rhie/Chow interpolation [24] is used to avoid odd/even pressure decoupling. As the code solves the incompressible flow equations, no equation of state exists for the pressure, and the SIMPLE algorithm of Patankar and Spalding [23] is used to enforce the pressure/velocity coupling. The EllipSys3D code is parallelized with MPI for execution on distributed memory machines, using a non-overlapping domain decomposition technique. For the current full rotor computations, a moving mesh technique based on analytical prescribed rotation is used [30]. The solution is advanced in time using a second-order iterative time-stepping (or dual time-stepping) method. In each global time step the equations are solved in an iterative manner, using underrelaxation. First, the momentum equations are used as a predictor to advance the solution in time. At this point in the computation the flow field will not fulfil the continuity equation. The rewritten continuity equation (the so-called pressure correction equation) is used as a corrector to make the predicted flow field satisfy the continuity constraint. This two-step procedure corresponds to a single subiteration, and the process is repeated until a convergent solution is obtained for the time step. When a convergent solution is obtained, the variables are updated and the computation continues with the next time step. For steady state computations the global time step is set to infinity and dual time stepping is not used. This corresponds to the use of local time stepping. To accelerate the overall algorithm, a three-level grid sequence is used in the steady state computations. The convective terms are discretized using a third-order upwind scheme, implemented using the deferred correction approach first suggested by Khosla and Rubin [16]. In each subiteration, only the normal terms are treated fully implicitly, while the terms from non-orthogonality and the variable viscosity terms are treated explicitly. Thus, when the subiteration process is finished, all terms are evaluated at the new time level. The three momentum equations are solved decoupled using

a red/black Gauss-Seidel point solver. The solution of the Poisson system arising from the pressure correction equation is accelerated using a multigrid method. In the present work the turbulence in the boundary layer is modelled by the $k-\omega$ SST model of Menter [18]. The equations for the turbulence model are solved after the momentum and pressure correction equations in every subiteration/pseudo time step. In the present work, all computations are performed using a $\gamma - \widetilde{Re}_\theta$ Laminar-turbulent transition model [28].

2.4.2 Mesh

The CFD surface mesh are first generated from the vortex method based on a NACA64418 profile. The central part of the blades have a spanwise discretization of the mesh points following a tangent hyperbolic distribution. The roots and the tips surfaces of each blades are automatically meshed using an in-house MATLAB based connector generator coupled with the commercial software Pointwise to generate the surface fitted domains, see Figure 2. Pointwise is run through a command line, using input files generated by the in-house MATLAB tool. Each blade is described using 36 blocks of 32^2 cells. The 3D mesh generation is done with a 3D version of hypgrid [29] an in-house hyperbolic mesh generation code. The minimum cell size is set to $\Delta x = 2.0 \cdot 10^{-7} R$, with R being the rotor radius. 161 layers are created based on a tangent hyperbolic distribution. The spherical outer boundary is located approximately 10 rotor diameter away. Some illustrations of the mesh generation on the 8% Winglet mesh are illustrated in Fig.2.
All the meshes considered in this work are composed of 540 blocks of 32^3 cells (17.7M cells).

2.4.3 Boundary Conditions

A zero gradient is enforced normal to the outlet of the downstream end of the spherical domain where the flow leaves the domain. At the upstream part of the spherical domain the undisturbed wind speed is specified. The surface of the blades are set as wall (no-slip) boundary conditions.

2.4.4 Computing Time

All the CFD computations are carried out on Thyra, a 64-bit linux cluster of Risø DTU. Each
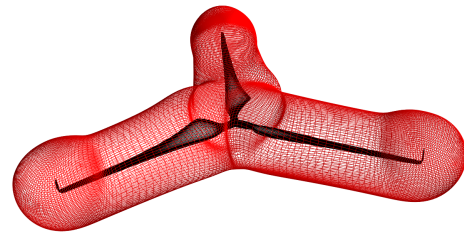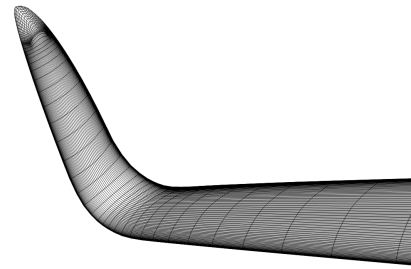

Figure 2: *Details of the computational mesh for the 8% winglet rotor case.*

simulation ran for about 12 hours on 20 CPUs in order to obtain a satisfying convergence.

3 Results

3.1 First validation: The effect of adding a winglet to a modern rotor

In order to further assess the performance of the lifting line based tools and to test the versions of the methods where the bound circulation is computed iteratively using the method described in 2.1.2, this subsection shows a comparison of the compared changes in power production and thrust force when adding a winglet of height 1.5% radii, plus and minus 90 degree cant angle (straight upwind/downwind) and zero sweep angle to a representative modern rotor. Johansen & Sørensen [15] described the aerodynamic investigation of a design change of the tip of a modern wind turbine blade by replacing the original tip with a winglet using computational fluid dynamics. Five different winglets were investigated. Of these five, we picked two having a fair performance, namely winglet 2 (the best upwind winglet) and

Table 2: Relative changes to the power production and thrust of a modern rotor at $\lambda = 7.6$ when adding upwind (WL2) or downwind winglets (WL5). Results from CFD (Johansen & Sørensen [15]) and lifting line free/prescribed wake models coupled to 3D geometry and 2D airfoil tables.

		$\frac{C_{P,WL}-C_{P,ref}}{C_{P,ref}}$	$\frac{C_{T,WL}-C_{T,ref}}{C_{T,ref}}$
	CFD [15]	1.38%	1.62%
Upwind winglet, WL2	Lifting line free wake	1.31%	1.36%
	Lifting line prescribed wake	1.00%	1.21%
	CFD [15]	1.71%	1.81%
Downwind winglet,WL5	Lifting line free wake	1.81%	1.73%
	Lifting line prescribed wake	1.32%	1.50%

winglet 5 (the downwind version of the same winglet) for validation of our lifting line based methods. The twist and chord distributions can be found in [15]. Using the geometry for the basic wing, the specific tip layouts in [15], and the 2D airfoil coefficients used in BEM methods for this rotor, the increments in power and thrust due to the addition of winglet 2 and winglet 5 to the original blade layout is evaluated at 10 m/s, corresponding to a tip speed ratio of $\lambda = 7.6$. It is noted that the actual bend from the main wing to the winglet is not considered in the shown lifting line results: the transition in the computations is simply a 90 degree sharp kink. Computations on other geometries have shown that this does not influence results significantly. Table 2 show the comparison of the key performance parameters of the rotors.

It is noted that the prescribed wake results correspond very well to the full CFD results and that the agreement in the case of the free wake results is excellent. This adds to the trust that this type of model can successfully predict the effects of winglets on wind turbine rotors.

To gain insight into the local behavior of the results of the lifting line based methods, Figure 3 compares the local nondimensional force coefficients on the modern rotor for the case without the winglet and the two different winglet cases. It is seen that the free and the prescribed wake results lie very close, indicating like the integral quantities, that the prescribed wake method performs quite well. The power production contribution from the winglet part for both winglet layouts are close to zero. The beneficial effect is seen at the outer part of the main blade, where the power production is significantly higher than without the winglet.
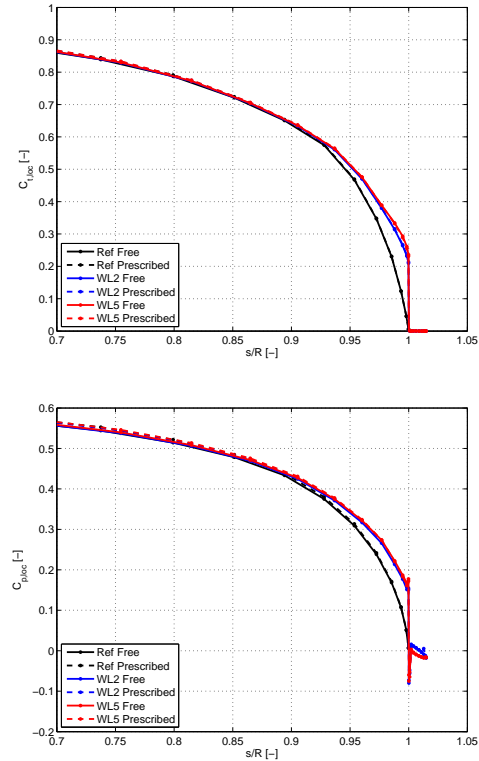

Figure 3: *Local thrust (upper) and power (lower) coefficients, $\tilde{C}_t$ and $\tilde{C}_p$ along the rotor blades for the modern rotor without and with the two different winglets. Comparison of CFD results and the lifting line based results.*

3.2 Comparison of performance of aerodynamic prediction tools

In this subsection, CFD and lifting line based results from analysis of basic and wingletted rotors designed with the lifting line based design method described earlier will be shown. The code EllipSys3D [19, 20, 26, 27] is used for the CFD investigations. The specific layout of the rotors shown here are based on free wake

solutions of the high loading cases with 0% winglet, 2% downwind winglet and 8% downwind winglets at a tip speed ratio of $\lambda = 8$. It was chosen to have the same airfoil all along the rotors, so as to make the evaluation of the performance more straightforward. The airfoil used on the rotors are the widely used 18% thick NACA 64-418 airfoils [1]. The point of maximum lift to drag values for this particular airfoil is at $\alpha_{Design} = 4^0$, where the lift coefficient is $C_{l,Design} = 0.8$. The lift to drag values used in the initial design lifting line computations is $C_l/C_d = 110$. Please note that the rotor designs derived and analyzed in this section is by no means 'structurally healthy', and will merely be used to highlight the capabilities of the lifting line tools and the aerodynamic behavior of the wingletted rotors. Figure 4 show
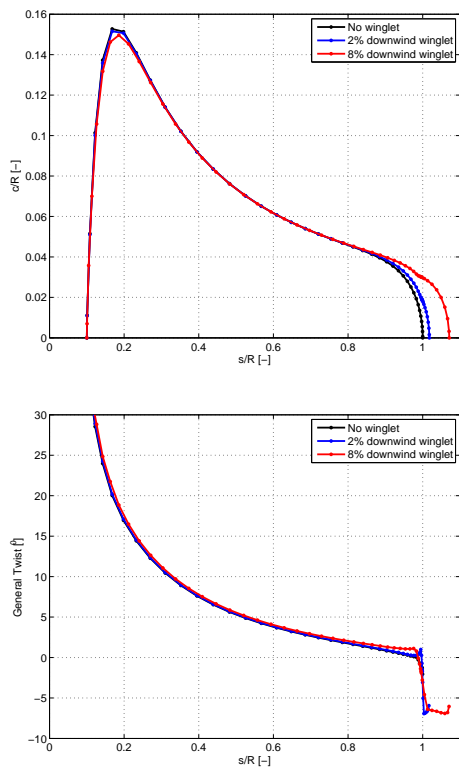

Figure 4: *Layout of the raw aerodynamic surfaces of the basic rotor, the 2% downwind winglet rotor and the 8% downwind winglet rotor. Upper:Chordlength. Lower:Angle of chord direction to the tangential direction. Transition from the main wing to the winglet part of the wing is a circular arc of radius a fourth of the winglet length.*

the layout of the aerodynamic part of the basic rotor, the 2% downwind winglet rotor and the 8% downwind winglet rotor. The layout is

determined by the chordlength and the angle of the chord direction to the tangential direction. The chordwise direction is normal to the local spanwise direction at all points on the rotor. The transition from the main wing to the winglet part of the wing is a circular arc of radius a fourth of the winglet length.
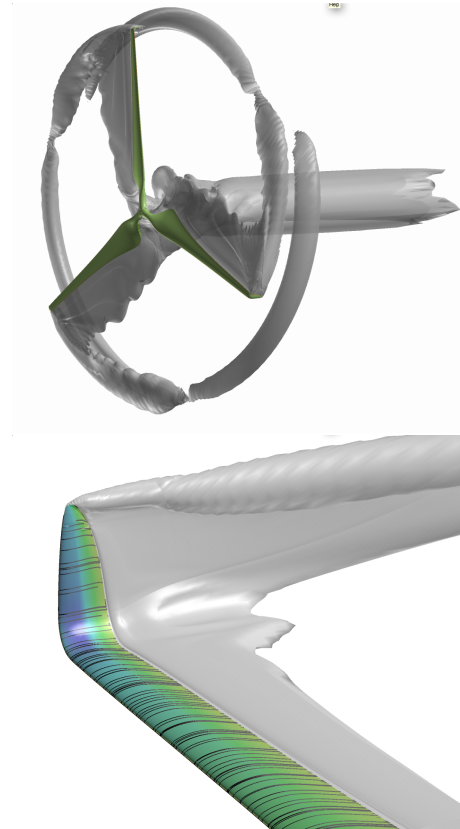

Figure 5: *Illustration of the flowfield around the 8% winglet rotor. Upper: Iso-vorticity surfaces. Lower: Relative pressures, iso-vorticity and surface streamlines.*

Figure 5 shows an illustration of the general features of the flowfield around the 8% rotor. It is noted that there is no separation in the tip region or close to the winglet. Figure 6, which show surface streamlines for the same case show the same thing. Also it can be seen that the only separated zone is on the suction side of the blade inboard of maximum chordlength. This verifies that the design strategy works well, and that the flow on the inner part of the wing is not disturbed by radial flow from separating regions.

Proceeding on to Figure 7, where local surface pressure coefficients for a multitude of crossections along the blades of the 8% winglet case are shown. Since the design strategy has been that the angle of attack and
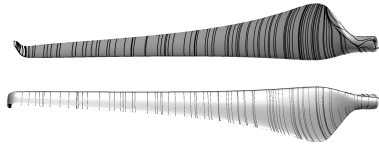
Figure 6: *Surface streamlines on the 8% winglet blade. Upper: suction side. Lower: pressure side.*
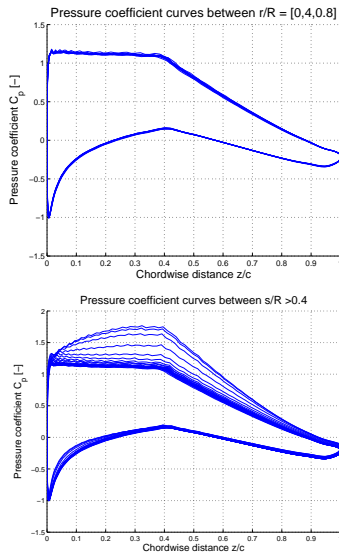

Figure 7: *Local surface pressure coefficients* $C_p(z, r) = (p(z, r) - p_\infty)/(0.5\rho(V_\infty^2 + (\Omega r)^2))$ *along the rotor blades.*

thereby design lift should be constant along the rotor, it is seen on the left figure that this is indeed the case for radii between $r/R = 0.4$ and $r/R = 0.8$. For some of the outer sections, however, the right figure show that the pressures deviate from the intended constant local pressure coefficient shape. Another view of this is shown in Figure 8 where iso-curves of the local surface pressures are shown for the 8% winglet case. As previously, if the design strategy works for the rotor, then the iso-lines of the local pressure coefficients should run only in the local spanwise direction. It is seen that this is certainly the case on the pressure side of the wing. However, it is also seen that there is an increased suction in the main-wing-to-winglet transition/bend region on the suction side. This location, along with the slight differences at the root region, where it is expected that the lifting line results (which are based on the large aspect ratio assumption) should not be able to describe the physics adequately, are seemingly the only places where the design

method is not working well. It is speculated that the algorithm for the self-induced velocities[3] in the lifting line method may be underestimating this effect
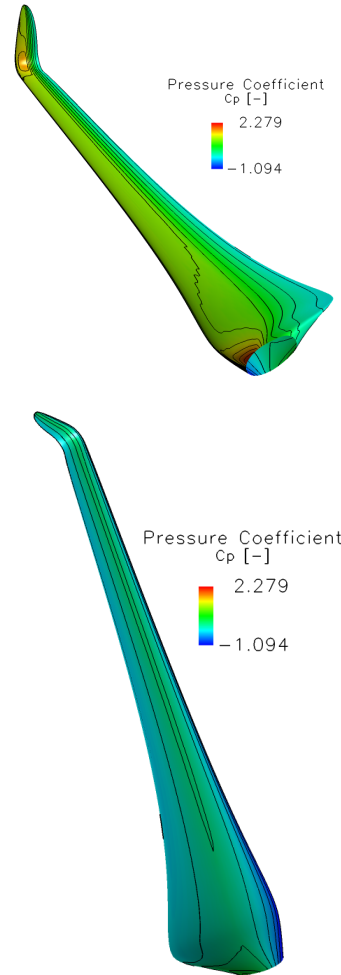

Figure 8: *Local surface pressure coefficient iso-curves on the 8% winglet blade. Upper: suction side. Lower: pressure side.*

In order to dig further into the evaluation of the comparison of the two ways of determining the aerodynamic loading, we compare the lifting line free wake results on which the rotor designs are based, and the CFD solutions on the rotors. To this end, we define the following dimesionless parameters for the local axial force, F_{axial}, local tangential/driving force, F_{drive} and local radial force, F_{radial}, (all per

---

[3]The self-induced velocities are the "extra" tangential induced velocity on the winglet due to the bound circulation on the main wing and the "extra" tangentially induced velocity on the main wing due to the bound circulation on the winglet. For the upwind rotor case the sign shifts such that there is a decrease in tangential velocity.

unit spanlength).

$$\tilde{C}_t(\tilde{s}) = \frac{N_B F_{axial}(\tilde{s})}{\pi \rho V_\infty^2 R \tilde{r}(\tilde{s})}$$

$$\tilde{C}_p(\tilde{s}) = \frac{N_B F_{drive}(\tilde{s})\lambda}{\pi \rho V_\infty^2 R} \qquad (16)$$

$$\tilde{C}_r(\tilde{s}) = \frac{N_B F_{radial}(\tilde{s})}{\pi \rho V_\infty^2 R \tilde{r}(\tilde{s})}$$

Note that non dimensional radius and spanlength parameter (positive from the root toward the tip along the local blade span)are defined as $\tilde{r} = r/R$ and $\tilde{s} = s/R$, respectively. It is seen that the local nondimensional thrust and power parameters correspond to the usual ones on the main part of the rotor. Defining the non dimensional loading this way for non straight blades means that the integral quantities C_T, C_P and C_R generally can be determined as

$$C_T = \int_{\tilde{s}_{root}}^{\tilde{s}_{tip}} 2\tilde{r}(\tilde{s})\tilde{C}_t(\tilde{s})d\tilde{s}$$

$$C_P = \int_{\tilde{s}_{root}}^{\tilde{s}_{tip}} 2\tilde{r}(\tilde{s})\tilde{C}_p(\tilde{s})d\tilde{s} \qquad (17)$$

$$C_R = \int_{\tilde{s}_{root}}^{\tilde{s}_{tip}} 2\tilde{r}(\tilde{s})\tilde{C}_r(\tilde{s})d\tilde{s}$$

The integral quantities are nondimensional versions of the integral thrust, T, power, P, and radial force on one blade, $F_{Radial,SingleBlade}$, are given as

$$C_T = \frac{T}{0.5\rho V_\infty^2 A}$$

$$C_P = \frac{P}{0.5\rho V_\infty^3 A} \qquad (18)$$

$$C_R = \frac{F_{Radial,SingleBlade} N_B}{0.5\rho V_\infty^2 A}$$

In addition to the local nondimensional force coefficients defined in Equation (16), a local quantity signifying the magnitude of the total local force

$$F_{total}(\tilde{s}) = \sqrt{F_{axial}^2(\tilde{s}) + F_{drive}^2(\tilde{s}) + F_{radial}^2(\tilde{s})} \qquad (19)$$

can be determined from the local nondimensional forces in Equation (16) as

$$\tilde{C}_f(\tilde{s}) = \frac{N_B F_{total}(\tilde{s})}{\pi \rho V_\infty^2 R \tilde{r}(\tilde{s})}$$

$$= \sqrt{\tilde{C}_t^2(\tilde{s}) + \tilde{C}_r^2(\tilde{s}) + \left(\frac{\tilde{C}_p(\tilde{s})}{\lambda \tilde{r}}\right)^2} \qquad (20)$$

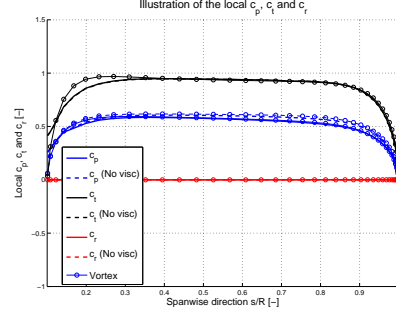Using the local nondimensional coefficients defined in Equations (16) and (20), we can

Figure 9: *Local thrust, power and radial force coefficients, $\tilde{C}_{t,loc}$, $\tilde{C}_{p,loc}$ and $\tilde{C}_{r,loc}$, along the rotor blades for the nonwingletted blade. Comparison of CFD results and the lifting line free wake results (circles).*

now compare the solutions along curved blade spans. Figure 9 show the comparison of the nondimensional load parameters along the basic wing with no winglet for the CFD computations and the free wake computation on which the design is based. It is seen that the agreement is excellent. Only a slight difference in between the methods is seen close to the root. Remember, that this difference is not very significant in terms of integral power and thrust, because the outer sections are weighted higher (see Equations (17)). It is also seen that the difference between the "raw" lifting line local power coefficient results excluding the viscous drag contribution (upper blue curve), corresponds well with the CFD results based on the integration of the pressure forces only. Even though the two are not supposed to be identical based on theoretical considerations[4], the result still indicates that the effects are taken into account in the correct fashion in the lifting line results. The integral C_T and C_P are given in table 3 for the non-wingletted rotor case for the CFD calculations and the free wake rotor design computations.

It is seen that the agreement on the thrust coefficient is excellent between the CFD and the rotor design computations, but that the agreement on the power coefficient is less good. This may be due to the a priori estimated lift to drag ratio of 110. Changing this ratio to 80 would result in a near perfect match between the power coefficients between the CFD and the free wake code results. Figure 10 show the 2D airfoil data used in the results from the coupled free/prescribed wake methods in this

---

[4]The 2D pressure coefficient is not identically equal to zero due to the displacement effect of the boundary layer.

Table 3: C_P and C_T values for the 0% winglet case. Results shown for the baseline free wake design computations, the CFD analysis, and the Free/Prescribed analysis based on geometry and 2D airfoil coefficients.

	C_P	C_T
Free wake rotor design computation	0.5099	0.8665
EllipSys3D	0.4948	0.8475
Free wake (geometry + 2D coeffs.)	0.5129	0.8600
Prescribed wake (geometry + 2D coeffs)	0.5162	0.8611

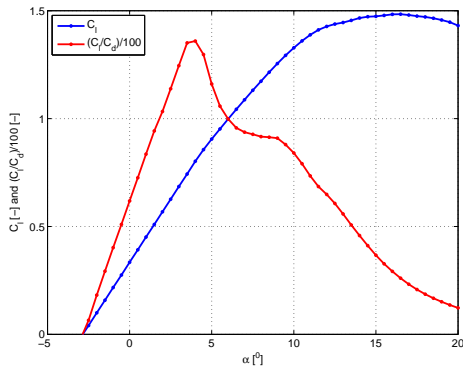comparison. The relatively higher lift to drag ra-

Figure 10: *Baseline 2D airfoil data for the NACA 64-418 airfoil at $Re = 6 \cdot 10^6$ computed using Rfoil.*

tios at the design angle of attack explains why the results from the free and prescribed wake methods coupled to the geometry of the rotor and 2D sectional airfoil behavior have relatively high power coefficients.

Further investigating the agreement between the two methods in the cases with winglets, Figures 11 to 13 show the comparison of the loadings for the rotors investigated.

Here we see that the agreement is quite good on most of the rotor, but that a slight difference is present at the bend to the winglet, where the forces in the CFD computations are higher than in the free wake code results. The general agreement between the results, however, is good. As for the case without winglet, it is observed that the predicted power coefficients are higher using the lifting line based tools than for the CFD computations. This may be caused by using unrealistically high lift to drag values in these computations. It is noticed that the effects with the increased loads at the bend is increased for the 8% winglet case compared to the 2% winglet case.

The integral C_T and C_P values for the computations with winglets are given in table 4.

It is seen that the trends for the winglet cases are the same as for the non-winglet cases. The agreement on the thrust coefficient is excellent, but that the agreement on the power coefficient is less good. Similar to the non-wingletted case this difference may be due to a wrong value used for the lift to drag ratio C_l/C_d.

4   Conclusions

The present report contains work on aerodynamic models capable of simulating non-straight wind turbine rotor blades. To this end the application of winglets on wind turbine rotors have been studied.

A free wake code and a newly developed prescribed wake lifting line algorithm has been used to analyze key features of rotors with winglets. The computational cost of the prescribed wake model is approximately three orders of magnitude lower than the free wake code for computational cases with a fine spatial discretization. The results obtained show that results from the prescribed wake model, which uses only the integral axial load on the rotor and the main geometry of the wing/winglet to
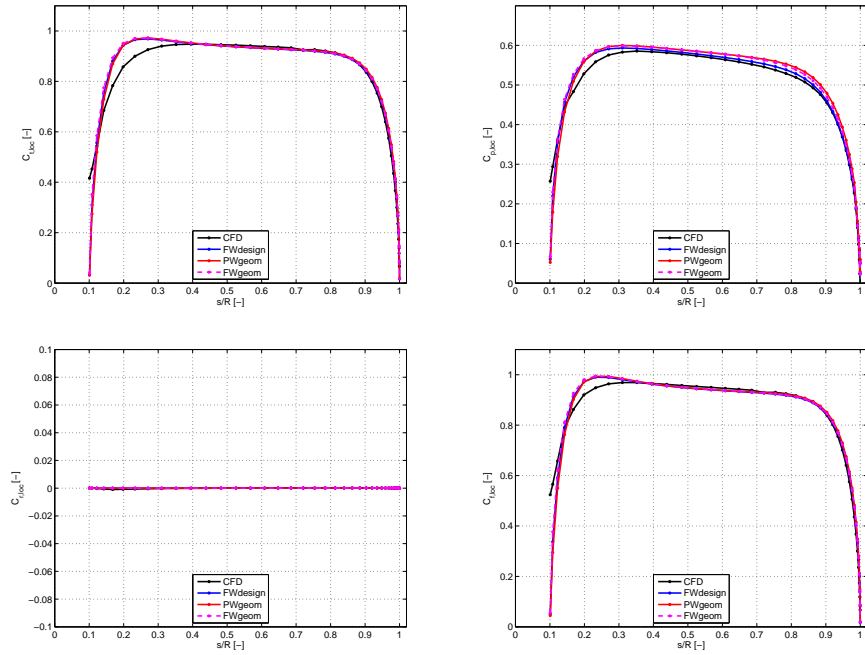
Figure 11: *Local thrust (upper left), power (upper right), radial force (lower left) and total force (lower right) coefficients, $\tilde{C}_t$, $\tilde{C}_p$, $\tilde{C}_r$, and $\tilde{C}_f$ along the rotor blades for the case without winglet. Comparison of CFD results and the lifting line based results.*
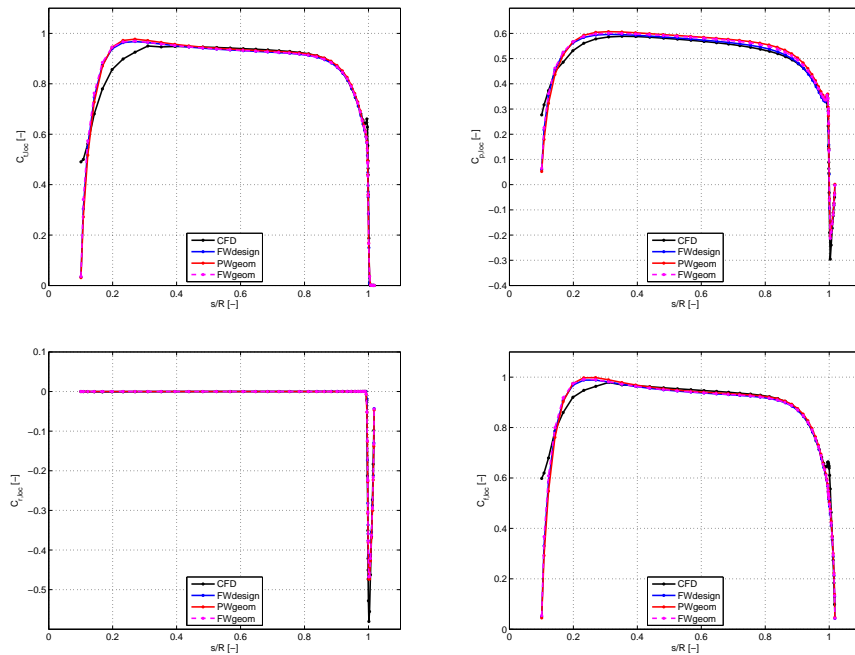

Figure 12: *Local thrust (upper left), power (upper right), radial force (lower left) and total force (lower right) coefficients, $\tilde{C}_t$, $\tilde{C}_p$, $\tilde{C}_r$, and $\tilde{C}_f$ along the rotor blades for the case with a 2% downwind winglet. Comparison of CFD results and the lifting line based results.*

estimate the wake shape, can produce results in good qualitative agreement with the physically more correct free wake model. The results indicate, however, that the power production estimated from these prescribed wake models may be erroneous if the load distribution along the wing is not similar to the one the model was calibrated for.
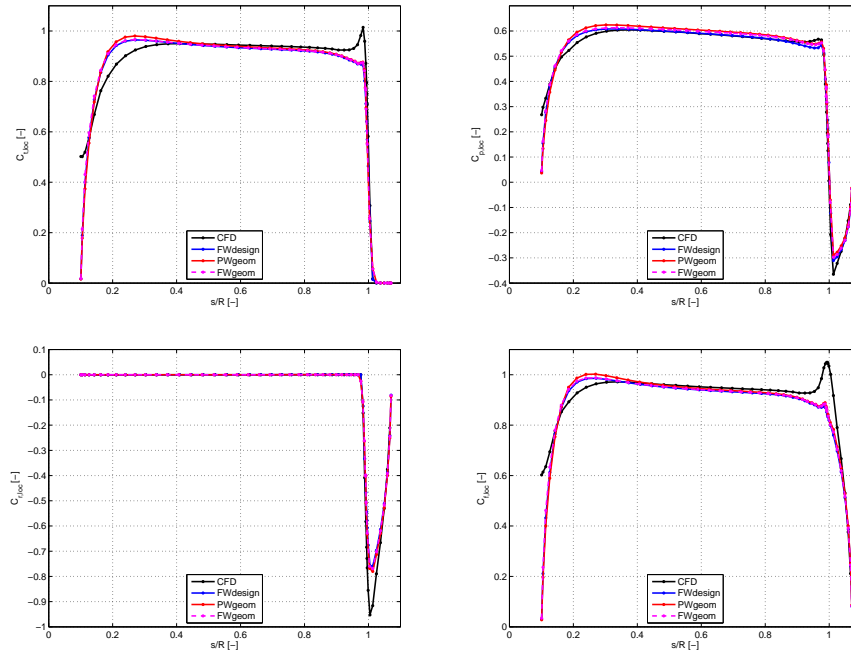
Figure 13: *Local thrust (upper left), power (upper right), radial force (lower left) and total force (lower right) coefficients, $\tilde{C}_t$, $\tilde{C}_p$, $\tilde{C}_r$, and $\tilde{C}_f$ along the rotor blades for the case with a 8% downwind winglet. Comparison of CFD results and the lifting line based results.*

Table 4: C_P and C_T values for the lifting line based computations and the CFD analysis of the winglet cases.

	$C_P 2\% winglet$	$C_T 2\% winglet$	$C_P 8\% winglet$	$C_T 8\% winglet$
Free wake rotor design computation	0.5226	0.8879	0.5323	0.9161
EllipSys3D	0.5069	0.8760	0.5225	0.9209
Free wake (geometry + 2D coeffs.)	0.5252	0.8804	0.5361	0.9089
Prescribed wake (geometry + 2D coeffs)	0.5302	0.8838	0.5420	0.9127

To complement the basic lifting line methods, a coupling algorithm has been implemented, such that both the free wake and the prescribed wake method is coupled to 2D airfoil coefficients and a generalized description of the rotor geometry suitable for non-straight rotors such as for instance for winglets. A validation of this coupling method against CFD results analyzing the effect of adding upwind and downwind winglets to a modern wind turbine rotor was undertaken, and it was shown that both lifting line tools performed very well for this case. Of the two, the computationally heavier free wake method was closest to the CFD results.

A method for determining the 3D rotor geometry for general non-straight rotor blades have been derived, and CFD computations from such rotor designs have been compared to the design goal, where a very good agreement was seen almost everywhere on the wings. In fact the only location where the CFD results deviate from the expected behavior is at the suction side of the rotor where the main rotor is bent into the winglet. Three cases (no winglet, 2% downwind winglet and 8% winglet) were analyzed with the 3D CFD code EllipSys3D, and the results were compared to the results from the lifting line based codes. It was found that the thrust values were closer to the design values than the power, but results indicate that the lift to drag values on which the in the lifting line results were based on may have been too high. A lift to drag value of between 80 and 90 would result in a very good agreement between lifting line and CFD simulation results. For the

investigated cases the prescribed wake simulations were in very good agreement with the computationally much more demanding free wake methods.

Acknowledgements

References

[1] Abbott, I.H. & von Doenhoff, A.E. *Theory of Wing Sections, including a summary of airfoil data* Dover, 1949.

[2] Van Bussel, G.J.W. *A momentum theory for winglets on horizontal axis wind turbine rotors and some comparison with experiments* Fourth IEA Symposium on the Aerodynamics of Wind Turbines, November 1990, Rome, Italy, Proc. edt. K.McAnulty, ETSU-N-118, Harwell, Didcot, U.K., January 1991

[3] Chattot, J.J., *Effects of Blade Tip Modifications on Wind Turbine Performance Using Vortex Model*, AIAA 2008-1315, 46th AIAA Aerospace Sciences Meeting and Exhibit, 7-10 January 2008, Reno, Nevada.

[4] Currin, H.D., Coton, F.N. & Wood, B. *Dynamic Prescribed Vortex Wake Model for AERODYN/FAST*, Journal of Solar Energy Engineering, Vol. 130. 7 p. August 2008.

[5] Gaunaa, M & Johansen, J. *Determination of the maximum aerodynamic efficiency of wind turbine rotors with winglets*, Journal of Physics 5, 2007 and oral presentation on 2nd EWEA,EAWE The Science of making Torque from Wind conference at DTU, 28-31 August 2007

[6] Gaunaa, M & Johansen, J. *Can CP be Increased by the Use of Winglets? – or – A Theoretical and Numerical Investigation of the Maximum Aerodynamic Efficiency of Wind Turbine Rotors with Winglets*, 46th AIAA Aerospace Sciences Meeting and Exhibit, 7-10 January 2008, Reno, Nevada.

[7] Gaunaa, M & Johansen, J. *Estimation of possible increase in Cp by use of Winglets*,

In: Bak, C. (ed.), Risø National Laboratory (DK). Wind Energy Department. Research in aeroelasticity EFP-2006. Risø-R-1611(EN) p. 47-62

[8] Gaunaa, M., Sørensen, N.N. & Døssing, M. *Prediction of steady aerodynamic performance of rotors with winglets using simple prescribed wake methods*, 49th AIAA Aerospace Sciences Meeting and Exhibit, January 2011, Orlando, Florida.

[9] Hansen, M.O.L. *Aerodynamics of wind turbines*, Second edition, Earthscan, 2008.

[10] Imamura, H. et al *Numerical Analysis of the Horizontal Axis Wind Turbine with Winglets*, JSME International Journal, Series B vol. 41 nr. 1, Feb 1998 JSME Tokyo Japan pp 170-176

[11] Johansen, J., Madsen, H, Aa., Gaunaa, M. and Bak C. *Design of a wind turbine rotor for maximum aerodynamic efficiency* Wind Energy, Vol. 12, 2009, p 261-273.

[12] Johansen, J., Gaunaa, M. & Sørensen, N.N. *Increased Aerodynamic Efficiency on Wind Turbine Rotors using Winglets* AIAA 2008-6728. 26th AIAA Applied Aerodynamics Conference, Honululu, Hawaii, August 18-21, 2008.

[13] Johansen, J.; Sørensen, N.N.; Aagaard Madsen, H.; Wen Zhong Shen; Okulov, V. *Advanced rotor aerodynamics - including tip and root aerodynamics*. In: Bak, C. (ed.), Risø National Laboratory (DK). Wind Energy Department. Research in aeroelasticity EFP-2005. Risø-R-1559(EN) p. 11-17

[14] Johansen, J. and Sørensen, N.N. *Numerical Analysis of Winglets on Wind Turbine Blades using CFD*, EWEC 2007 Conference proceedings, Madrid, Spain

[15] Johansen, J. & Sørensen, N.N. *Aerodynamic investigation of Winglets on Wind Turbine Blades using CFD*, Technical Report Risø-R-1543(EN), Risø National Laboratories, 2006.

[16] Khosla, P.K. & Rubin, S.G. *A diagonally dominant second-order accurate implicit scheme.* Computers Fluids, 2:207–209, 1974.

[17] Madsen, H.Aa., Mikkelsen, R., Johansen, J., Bak, C., Øye, S. & Sørensen, N.N

Inboard rotor/blade aerodynamics and its influence on blade design. Chapter in Risøtechnical report: Research in aeroelasticity EFP-2005. Ed. Bak, C. Risø-R-1559(EN), Roskilde, Denmark, May 2006. p.19-39.

[18] Menter, F.R. *Zonal Two Equation k-ω Turbulence Models for Aerodynamic Flows*. AIAA Paper 93-2906, 1993

[19] Michelsen J.A. *Basis3D - a Platform for Development of Multiblock PDE Solvers.* Technical Report AFM 92-05, Technical University of Denmark, 1992

[20] Michelsen J.A. *Block structured Multigrid solution of 2D and 3D elliptic PDE's.* Technical Report AFM 94-06, Technical University of Denmark, 1994

[21] Müller R.H.G & Staufenbiel R *The Influence of Winglets on Rotor Aerodynamics* Vertica Vol. 11, No. 4, p.601-618. 1987

[22] Müller R.H.G *Winglets on Rotor Blades in Forward Flight – a Theoretical and Experimental Investigation* Vertica Vol. 14, No. 1, p.31-46, 1990.

[23] Patankar, S.V. and Spalding, D.B., *A Calculation Prodedure for Heat, Mass and Momentum Transfer in Three-Dimensional Parabolic Flows.* Int. J. Heat Mass Transfer, 15:1787, 1972.

[24] Rhie, C.M. *A numerical study of the flow past an isolated airfoil with separation.* PhD thesis, Univ. of Illinois, Urbana-Champaign, 1981.

[25] Sant, T. van Kuik, G. & van Bussel, G.J.W. *Estimating the Angle of Attack from Blade Pressure Measurements on the NREL Phase VI Rotor Using a Free Wake Vortex Model: Axial Conditions*. Wind Energy, Vol. 9, 2006, p 549-577.

[26] Sørensen N.N. *General Purpose Flow Solver Applied to Flow over Hills.* Risø-R-827-(EN), Risø National Laboratory, Roskilde, Denmark, June 1995

[27] Sørensen N.N., Michelsen J.A., Schreck, S. *Navier-Stokes predictions of the NREL phase VI rotor in the NASA Ames 80 ft X 120 ft wind tunnel.* Wind Energy. 2002;5(2-3):151-169.

[28] Sørensen, N.N. *Cfd modelling of laminar-turbulent transition for airfoils and rotors using the gamma-(re)over-tilde (theta) model.* Wind Energy, 12(8):715–733, 2009.

[29] Sørensen, N.N., *HypGrid2D, a 2-D mesh generator.* Technical report, Risø-R-1035(EN), Risoe National Laboratory, 1998.

[30] Sørensen, N.N. *computations using a 'Steady State' moving mesh.* IEA Joint Action Committee on aerodynamics, Annex XI and 20. Aero experts meeting, Pamplona (ES), 25-26 May 2005.

[31] Øye, S. *A simple vortex model.* In Proc. of the third IEA Symposium on the Aerodynamics of Wind Turbines, ETSU, Harwell, 1990, p. 4.1-4.15.

[32] *The On-Line Encyclopedia of Integer Sequences.* http://www.research.att.com/ njas/sequences/A049773